

Correction

BIOPHYSICS AND COMPUTATIONAL BIOLOGY

Correction for “Emergence of ion channel modal gating from independent subunit kinetics,” by Brendan A. Bicknell and Geoffrey J. Goodhill, which appeared in issue 36, September 6, 2016, of *Proc Natl Acad Sci USA* (113:E5288–E5297; first published August 22, 2016; 10.1073/pnas.1604090113).

The authors note that on page E5292, left column, second full paragraph, line 6, “ $3b_3$ ” should instead appear as “ $3b_{11}$.”

www.pnas.org/cgi/doi/10.1073/pnas.1619297114

Emergence of ion channel modal gating from independent subunit kinetics

Brendan A. Bicknell^{a,b} and Geoffrey J. Goodhill^{a,b,1}

^aQueensland Brain Institute, The University of Queensland, St. Lucia, QLD 4072, Australia; and ^bSchool of Mathematics and Physics, The University of Queensland, St. Lucia, QLD 4072, Australia

Edited by Richard W. Aldrich, The University of Texas at Austin, Austin, TX, and approved July 13, 2016 (received for review March 14, 2016)

Many ion channels exhibit a slow stochastic switching between distinct modes of gating activity. This feature of channel behavior has pronounced implications for the dynamics of ionic currents and the signaling pathways that they regulate. A canonical example is the inositol 1,4,5-trisphosphate receptor (IP₃R) channel, whose regulation of intracellular Ca²⁺ concentration is essential for numerous cellular processes. However, the underlying biophysical mechanisms that give rise to modal gating in this and most other channels remain unknown. Although ion channels are composed of protein subunits, previous mathematical models of modal gating are coarse grained at the level of whole-channel states, limiting further dialogue between theory and experiment. Here we propose an origin for modal gating, by modeling the kinetics of ligand binding and conformational change in the IP₃R at the subunit level. We find good agreement with experimental data over a wide range of ligand concentrations, accounting for equilibrium channel properties, transient responses to changing ligand conditions, and modal gating statistics. We show how this can be understood within a simple analytical framework and confirm our results with stochastic simulations. The model assumes that channel subunits are independent, demonstrating that cooperative binding or concerted conformational changes are not required for modal gating. Moreover, the model embodies a generally applicable principle: If a timescale separation exists in the kinetics of individual subunits, then modal gating can arise as an emergent property of channel behavior.

ion channel | modal gating | inositol 1,4,5-trisphosphate receptor | Markov model | calcium signaling

The regulation of cytosolic Ca²⁺ ion concentration is fundamental to a wide range of cellular processes, including immune responsiveness (1), synaptic plasticity (2), axon guidance (3), and apoptosis (4). Several processes contribute to the spatial and temporal dynamics of Ca²⁺, such as diffusion and buffering, exchange with the extracellular space, and uptake and release from intracellular stores. The inositol 1,4,5-trisphosphate receptor (IP₃R) ion channel is a key component in shaping Ca²⁺ signals, as it controls the local efflux from the endoplasmic reticulum (ER), where Ca²⁺ is sequestered at high concentration (5, 6). The IP₃R is a ligand-gated channel, subject to regulation by binding of IP₃ and also Ca²⁺ itself. Recently, it has been revealed that the main method of ligand regulation is to affect a slow switching between distinct levels of channel activity—a phenomenon known as modal gating (7–9). IP₃R modal gating has pronounced implications for the dynamics of Ca²⁺ release events (10), and its dysfunction has been implicated in the pathogenesis of familial Alzheimer's disease (11, 12). A detailed understanding of this important feature of IP₃R behavior is therefore crucial for unraveling the complexity of Ca²⁺ signaling and its role in cell function and disease. Modal gating has been observed in the kinetics of many other ion channels, such as K⁺ (13–18), Cl[−] (19), glutamate receptors (20, 21), plasma membrane Ca²⁺ (22–24), and ryanodine receptor Ca²⁺ (25, 26). However, the underlying biophysical basis of modal gating in the IP₃R and most other channels remains unknown.

Structurally, IP₃Rs are large, homotetrameric proteins of which there are three main subtypes. Binding of IP₃ to a cytosolic domain

contributes to channel activation via a conformational change in channel subunits. However, the location and action of Ca²⁺ binding sites (believed to be at least two per subunit) are unresolved (27). Here, we focus on type 1 IP₃Rs, which are the main neuronal subtype and for which a range of single-channel kinetic properties have been determined from within the same cell type (Sf9) (7, 28, 29). Under fixed ligand conditions, the type 1 IP₃R gates in three modes that are characterized by high, intermediate, and low open probability. The within-mode open probabilities are approximately ligand independent, whereas the proportion of time spent in each mode is regulated by the IP₃ and Ca²⁺ concentration (7, 30), leading to the well-described bell-shaped open probability curve (28, 31, 32). In contrast to the slow switching between modes, the channel exhibits individual opening and closing events of millisecond durations and responds rapidly to changing ligand concentrations (29).

The challenge in developing a complete biophysical understanding of the IP₃R is to bridge the gap between the microscopic picture that is evolving from molecular studies and the macroscopically observable statistics of channel gating. Markov models of channel gating are an excellent tool for approaching this problem in quantitative terms. It is clear that any description of the IP₃R must encompass stochastic dynamics over several timescales and ideally be relatable to the underlying biology. Stochastic implementations of the classic De Young–Keizer (DYK) model assume four independent subunits and explicitly incorporate ligand binding and conformational change (33, 34). Variants of this scheme have been widely used in studies of the IP₃R and Ca²⁺ dynamics (35–45), although none exhibit modal gating. This raises the question of whether this intuitive, bottom-up approach is compatible with current knowledge of IP₃R regulation. Whereas two recent top-down IP₃R models were able to fit this feature of the data (46, 47), the coarse graining of channel states precludes predictions as to its origin at finer spatial scales.

Significance

Many key features of the behavior of cells are controlled by ion channels—pores in cell membranes that are sometimes open and sometimes closed. It is therefore critically important to understand what controls these opening and closing events. This is challenging because ion channels exhibit stochastic dynamics over several timescales, from the rapid kinetics of a single opening to the slow switching between distinct levels of activity known as modal gating. By mathematically modeling the basic biophysical events that control ion channel opening, we introduce a new principle for understanding the origin of modal gating. Although we focus on the inositol 1,4,5-trisphosphate receptor channel, the framework can be applied more generally to other ion channels.

Author contributions: B.A.B. and G.J.G. designed research; B.A.B. performed research; and B.A.B. and G.J.G. wrote the paper.

The authors declare no conflict of interest.

This article is a PNAS Direct Submission.

¹To whom correspondence should be addressed. Email: g.goodhill@uq.edu.au.

This article contains supporting information online at www.pnas.org/lookup/suppl/doi:10.1073/pnas.1604090113/-DCSupplemental.

Here, we show how modal gating can emerge from subunit-based models of ion channel gating. We propose that modal gating in the IP₃R is a consequence of a timescale separation in the kinetics of individual subunits. Motivated by the DYK approach, we first introduce two simple motifs for subunit kinetics, where the first one gives rise to channel bursting, and the second one exhibits slow modal gating as an emergent statistical property. We show that the subunit kinetics induce a natural partition of the full channel state space that underlies three distinct modes of activity. We then use these ideas as a basis for constructing a stochastic model of the type 1 IP₃R, comprehensively fitted to both equilibrium and transient kinetic data. The result is a bottom-up model that transparently describes all aspects of gating behavior in terms of elementary binding events and conformational changes. In this way we show that minimal coupling is required between the kinetics of IP₃R subunits to account for the full complexity of gating patterns. Although we use the IP₃R as a model problem, the general principle may be applicable to other ligand-regulated channels.

Results

We model a channel subunit of the IP₃R as a continuous-time Markov chain with a discrete state space corresponding to binding occupancy of ligand molecules and protein conformation. We assume that each of the four subunits that compose the channel are identical and independent and have a single active state that becomes accessible after ligand binding. Previous DYK schemes assume that the channel opens when at least three of four subunits are active (35–45). This yields a channel with multiple open states, consistent with experimental observations (37). However, by itself this rule is inconsistent with the recent discovery that channel opening requires all subunits to be bound by IP₃ (48). Therefore, we impose the additional constraint that the channel must be fully occupied by activating ligands to open. We assume further that binding of Ca²⁺ to the inhibitory site of a single subunit is sufficient to close the channel. The stoichiometry of Ca²⁺ regulation of the IP₃R is unknown; however, we found that these assumptions were the most consistent with observed features of channel gating. We return to address the implications and interpretation of these assumptions in *Discussion*.

We denote the states of a subunit Markov chain by X_i ($i = 1, \dots, n$) and the generator matrix by Q . Detailed balance is assumed and enforced with Kolmogorov's criterion (that the products of forward and reverse rates around all cycles are equal). The equilibrium distribution of subunit state is denoted by the vector w , given by the solution to

$$wQ = 0, \quad [1]$$

subject to the constraint $\sum_{i=1}^n w_i = 1$. In general, we denote the set containing the single active state by \mathcal{A} and the set of unliganded or inhibited states by \mathcal{C} . We denote by $w_{\mathcal{A}}$ and $w_{\mathcal{C}}$ the probability that a subunit occupies \mathcal{A} or \mathcal{C} , respectively. With these definitions, the equilibrium channel open probability is given by

$$P_{\text{O}} = w_{\mathcal{A}}^4 + 4w_{\mathcal{A}}^3(1 - w_{\mathcal{A}} - w_{\mathcal{C}}), \quad [2]$$

where the first and second terms account for channel openings involving four and three active subunits, respectively.

Bursting Motif. We first consider a four-state motif for subunit kinetics in the presence of a saturating IP₃ concentration. This motif is a subset of the 10-state model structure of ref. 37, which we have simplified by removing IP₃ dependence and assuming sequential binding of activating and inhibitory Ca²⁺. This simple description captures the essential features of Ca²⁺ regulation and bursting behavior. The diagram for the Markov chain is shown in Fig. 1. State transitions corresponding to a change in binding occupancy are described by mass action kinetics with rate constants a_i, b_i ($i = 1, 2$) and c , the cytosolic Ca²⁺

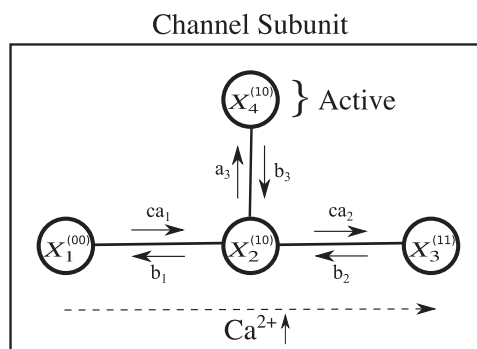


Fig. 1. Single-subunit Markov chain diagram of the bursting motif. Each subunit consists of four states X_i representing the binding occupancy of activating (first superscript) and inhibitory (second superscript) Ca²⁺ and conformational change to an active state (X_4). Ligand-dependent transition rates are described by mass action kinetics with rate constants a_i, b_i ($i = 1, 2$) and c being the cytosolic Ca²⁺ concentration. With increasing Ca²⁺ concentration, the equilibrium distribution of subunit state shifts in the direction of the dashed arrow. The channel opens when at least three subunits are in the active state and neither X_1 nor X_2 is occupied. Fast rates of ligand-independent conformational change (a_3, b_3) give rise to channel bursting. Parameter values are given in Table S1.

concentration. A subunit in state X_2 , which corresponds to an occupied activating Ca²⁺ site and an unoccupied inhibitory site, can undergo a ligand-independent conformational change to the active state X_4 with forward and reverse rate constants a_3, b_3 . We make order of magnitude estimates of parameters, chosen such that the conformational change to the active state is much faster than ligand-dependent transitions (Table S1). The difference in transition rates gives rise to bursts of channel openings, as subunits flicker between X_2 and X_4 , interspersed with gaps when a subunit has made a slower ligand-dependent transition to X_1 or X_3 . As in the original DYK model, the characteristic bell-shaped Ca²⁺ dependence of the open probability curve arises because the inhibitory site is of much lower affinity than the activating site and therefore suppresses activity only when the concentration is sufficiently high.

Following ref. 37, we calculate the equilibrium open probability (Eq. 2) by considering the unnormalized probabilities q_i of subunit states relative to the base state X_1 (so $q_1 = 1$). As there is a balance of probability flux between adjacent states, each q_i can be determined iteratively along any path from X_1 . This gives, for example, $q_3 = c^2/K_1K_2$, where $K_i = b_i/a_i$ are the dissociation constants. Summing over the q_i gives the normalization factor

$$Z = 1 + \frac{c}{K_1} + \frac{c^2}{K_1K_2} + \frac{c}{K_1K_3}. \quad [3]$$

The open probability is then determined from the quantities $w_{\mathcal{A}} = c/K_1K_3Z$ and $w_{\mathcal{C}} = (1 + c^2/K_1K_2)(1/Z)$. At equilibrium, the mean open and closed times can be approximated as

$$\langle \tau_{\text{O}} \rangle = \frac{P_{\text{O}}}{J}, \quad \langle \tau_{\text{C}} \rangle = \frac{1 - P_{\text{O}}}{J}, \quad [4]$$

respectively, where $J = 4w_{\mathcal{A}}^3(1 - w_{\mathcal{A}} - w_{\mathcal{C}})(3b_3 + b_1 + ca_2)$ is the total flux out of the open channel state in which there are three active subunits (37, 40). It is the equilibrium properties given by Eqs. 2 and 4 that have been predominantly used to fit previous subunit-based models of the IP₃R channel. We now decompose these further to isolate the contributions from bursts and gaps.

Timescale Separation. In their seminal work on the aggregated Markov model approach to channel gating, the authors of ref. 49 demonstrated that rich kinetic behavior could be attributed to a timescale separation that partitions the channel into open

states and both short- and long-lived closed states. We consider an analogous principle, although we apply it at the level of a channel subunit. We define the set \mathcal{B} as the union of \mathcal{A} and the set of any “short-lived” nonactive states (those from which the active state will be reached in the order of ~ 10 ms). In this motif, $\mathcal{B} = \{X_2, X_4\}$ for most values of c , although this extends to include X_1 when c becomes large ($\sim 20 \mu\text{M}$) (Fig. 1). We use w_B to denote the probability that a given subunit is in \mathcal{B} . The occupancy of \mathcal{B} partitions the channel state space naturally into two subsets that we identify with high (H) and low (L) modes of activity:

$$\text{H: } \{4 \text{ subunits in } \mathcal{B}\}, \text{ L: } \{\leq 3 \text{ subunits in } \mathcal{B}\}.$$

In this motif, H and L are simply the regions of the state space associated with channel bursts and burst-terminating gaps, respectively. For c not too large, we have

$$w_B = w_2 + w_A = \frac{(1 + K_3)c}{K_1 K_3 Z}, \quad [5]$$

which gives the probabilities π of the channel being within either H or L as

$$\pi^H = w_B^4, \quad \pi^L = 1 - w_B^4. \quad [6]$$

The kinetics within bursts are mostly determined by the rates of fast conformational change a_3, b_3 . For a subunit that is in \mathcal{B} , the conditional probability that it is active is given by

$$w_{\mathcal{A}|\mathcal{B}} = \frac{w_A}{w_B} = \frac{1}{1 + K_3}. \quad [7]$$

For large enough c that \mathcal{B} includes X_1 there is an additional term $K_1 K_3 / c$ in the denominator of Eq. 7, but as K_1 and K_3 are small, this contribution has little influence. A similar argument shows that the conditional probability $w_{\mathcal{C}|\mathcal{B}}$ that a subunit is in \mathcal{C} , given it is in \mathcal{B} , is always close to zero. This result yields conditional open probabilities for H and L that are effectively independent of ligand concentration,

$$P_O^H = w_{\mathcal{A}|\mathcal{B}}^4 + 4w_{\mathcal{A}|\mathcal{B}}^3(1 - w_{\mathcal{A}|\mathcal{B}} - w_{\mathcal{C}|\mathcal{B}}), \quad P_O^L = 0. \quad [8]$$

Because channel opening is permissible only in H, the mean open time within a burst is simply given by Eq. 4 (given the parameters in Table S1, $\langle \tau_O \rangle \sim 25$ ms). Each opening begins in a channel configuration with three active subunits and one in state X_2 . Ignoring the small contribution from burst termination, the expected waiting time until the next transition is $1/(a_3 + 3b_3) \sim 5$ ms. With probability $3b_3/(a_3 + 3b_3)$ this results in channel closing. Otherwise, the channel enters the configuration with four active subunits and remains open for a further expected ~ 35 ms to yield the total $\langle \tau_O \rangle$. Thus, the fast conformational change in the model induces similarly fast gating behavior at the channel level and two discernible open states.

The dynamic switching between H and L is controlled instead by the ligand-dependent transitions. If we consider the states in \mathcal{B} to be in fast equilibrium, then the mean burst length can be approximated as the expected time for the first subunit to leave \mathcal{B} , $\tau^H = 1/4(1 - w_{\mathcal{A}|\mathcal{B}})(b_1 + ca_2) \sim 250$ ms. The subsequent dwell time in L is then determined by the time taken for all subunits to return to a permissive liganded state. Therefore, the characteristic P_O curve arises from ligand regulation of the proportion of time spent in either bursting or quiescent channel states, described intuitively by $P_O = \pi^H P_O^H$ (Fig. S1).

This analysis suggests that the essential ingredients for modal gating are present in this simple motif. However, it cannot account for the slow regulation of IP₃R modes characterized by

ref. 7, where, for example, L-mode dwell times are on the order of seconds even in the high P_O ligand concentration regime. Attempting to address this by simply scaling the rate constants (keeping K_i constant) to give slower ligand regulation is inconsistent with the fast response latencies observed experimentally (29). Moreover, there is no capacity for a third, intermediate level of activity. This motivates the introduction of a slow timescale to the subunit kinetics to regulate the modal occupancies. We show that the intermediate mode arises as a direct consequence.

Modal Gating Motif. The ligand-independent conformational change that we have included in the previous motif is supported by experimental observations of channel flickering and reduced sensitivity to Ca^{2+} during bursts (37). We make a simple extension to the bursting motif by assuming that there exists a protein conformation that suppresses this activating step (Fig. 2). Modal gating of the channel emerges if suppression, by any Ca^{2+} -independent mechanism such as phosphorylation or binding of accessory proteins, occurs on a slow timescale.

The modal gating motif illustrates a key principle. There are three timescales present in the subunit kinetics: fast conformational change to an active state ($a_3 \sim 100 \text{ s}^{-1}$), ligand-dependent transitions ($ca_1, b_1, ca_2, b_2 \sim 1-10 \text{ s}^{-1}$), and a slow transition to a set of sequestered states ($a_4, b_4 \sim 0.1 \text{ s}^{-1}$), where subunit activation is suppressed. This transition to the sequestered states regulates the availability of channel subunits to enter into \mathcal{B} and thus slowly controls the overall level of channel activity.

We scale the rates of activation and inhibition to retain approximately the same total open probability curve as the bursting motif (Fig. 3A). Equilibrium properties are calculated as before, in this case with the normalization factor

$$Z = 1 + \frac{c}{K_1} + \frac{c^2}{K_1 K_2} + \frac{c}{K_1 K_3} + \frac{1}{K_4} + \frac{c}{K_1 K_4} + \frac{c^2}{K_1 K_2 K_4}, \quad [9]$$

and $w_C = (1 + 1/K_4)(1 + c^2/K_1 K_2)(1/Z)$ accounting for the additional states.

This motif generates an additional open channel configuration to the two that mediate H-mode openings in the previous model. In this configuration, where a single subunit is sequestered in state X_6 , channel openings involve three active subunits only,

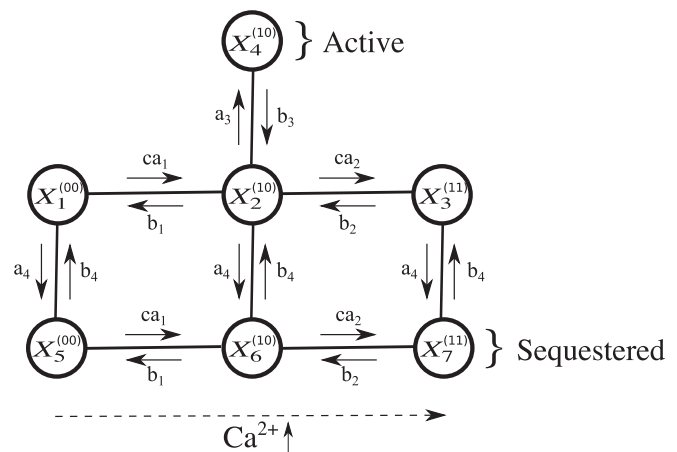


Fig. 2. Markov chain diagram of the modal gating motif. In this extension of the bursting motif, the conformational change to the active state can be suppressed by a slow Ca^{2+} -independent process, represented by transition to states X_5, X_6, X_7 . Modal gating emerges when the rates of this transition (a_4, b_4) are slow relative to Ca^{2+} binding and activation kinetics. Parameter values are given in Table S2.

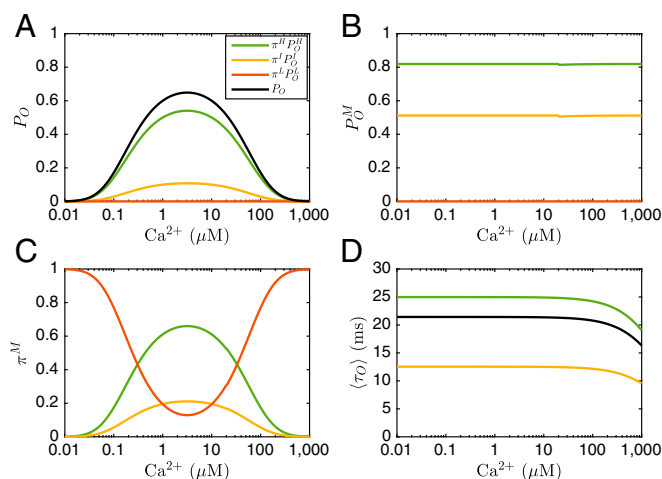


Fig. 3. Decomposition of equilibrium properties of the modal gating motif. The channel state space can be partitioned into subsets corresponding to H-mode (green), I-mode (yellow), and L-mode (red) activity. (A) The total channel open probability P_O (black line) is the sum of two components associated with H and I modes, as given by Eq. 12. (B) Within-mode open probabilities P_O^M are ligand independent. (C) The proportion of time spent in each mode π^M is strongly ligand dependent. (D) The mean open time $\langle\tau_O\rangle$ (black line) is the weighted sum of two components associated with H and I modes. Channel openings in H mode last much longer on average than those in I mode.

yielding a kinetically distinct intermediate mode. We define $\mathcal{S} = \{X_6\}$ and, analogous to the definition of \mathcal{B} , extend this to $\mathcal{S} = \{X_5, X_6\}$ when c is large. Taking the slow sequestration into account, the channel state space is partitioned into three subsets associated with H, intermediate (I), and L modes of activity:

$$\begin{aligned} \text{H: } & \{4 \text{ subunits in } \mathcal{B}\}, \text{ I: } \{3 \text{ subunits in } \mathcal{B}\} \cap \{1 \text{ subunit in } \mathcal{S}\}, \\ \text{L: } & \{\leq 3 \text{ subunits in } \mathcal{B}\} \setminus \{\text{I}\}. \end{aligned}$$

These are occupied with ligand-dependent probabilities

$$\pi^H = w_B^4, \quad \pi^I = 4w_B^3 w_S, \quad \pi^L = 1 - \pi^H - \pi^I. \quad [10]$$

The conditional open probability for I is given by

$$P_O^I = w_{A|B}^3 (1 - w_{C|S}), \quad [11]$$

with the expressions for H and L given by Eq. 8. This result gives the decomposition of the total channel open probability

$$\begin{aligned} P_O &= \pi^H P_O^H + \pi^I P_O^I \\ &= w_A^4 + 4w_A^3 (1 - w_A - w_C), \end{aligned} \quad [12]$$

consistent with Eq. 2. As the open probabilities within each mode are independent of ligand concentration (Fig. 3B, with these parameters, $P_O^H \sim 0.8$ and $P_O^I \sim 0.5$), the P_O curve can be seen to arise because of a shift in the probability of being within H, I, and L (Fig. 3C).

The mean open time (Eq. 4) can be decomposed similarly by conditioning on the state in which opening begins (*SI Materials and Methods*). For I-mode openings, we find $\langle\tau_O^I\rangle \sim 1/3b_3$, which is simply the expected waiting time for one of three subunits to leave the active state. By contrast, H-mode openings are longer by a factor of 2, $\langle\tau_O^H\rangle \sim 2/3b_3$, which, as in the bursting motif, reflects the fact that sojourn to the channel state with four active subunits is likely before closing (Fig. 3D).

Simulations. Gillespie simulations of channel gating exhibit the main qualitative features of experimental current traces (Fig. 4). At subactivating (0.1 μM) and inhibitory (100 μM) ligand concentrations, the channel gates in sequences of bursts and gaps. In the optimal, high P_O regime (1 μM), although the channel is predominantly open, the motif allows for abrupt channel closures lasting several seconds. The presence of a high and also intermediate mode of activity is clearly revealed by burst filtering (7), where channel closings shorter than a small threshold value are ignored. In the example trace in Fig. 5, the channel initially exhibits a period of intermediate open probability that is insensitive to filtering, and then after several seconds of quiescence it switches to a high open probability mode that is sensitive to filtering. Mode switches occur as subunits slowly transition in and out of the sequestered states.

The signature of this slow regulation is seen in the autocorrelation function of the binary (open/closed) channel state, which we computed from a 10^4 s simulated trace at 1 μM Ca^{2+} concentration (Fig. S2). This result shows that correlations in channel activity persist for seconds. This is because the probability of the channel state is biased by the underlying gating mode, leading to correlated activity on the timescale of mode switches. For comparison, we removed the slowest timescale by scaling up the rates a_4, b_4 of the sequestering transition. This leaves all equilibrium properties unchanged, but gives channel kinetics analogous to the bursting motif. In this case the slow modal gating disappears, and correlations persist only for as long as a single Ca^{2+} binding event.

This general motif provides a basis by which modal gating can be understood at the level of subunit kinetics. The behavior of individual subunits combines to yield a channel that stochastically switches between three interconnected modes. Channel

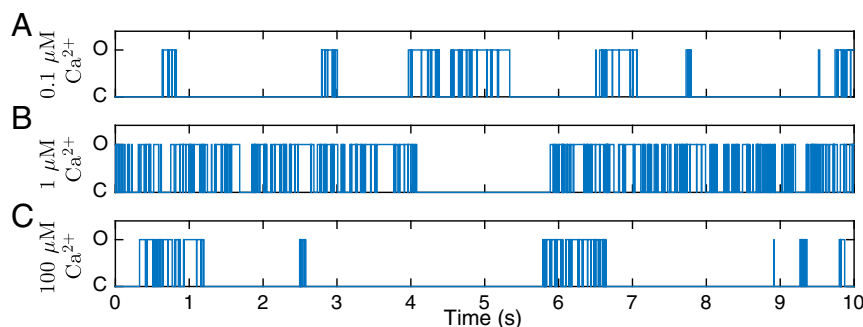


Fig. 4. Examples of simulated channel gating in fixed Ca^{2+} concentrations in the subactivating (0.1 μM), optimal (1 μM), and inhibitory (100 μM) regimes. The vertical axis in each trace denotes an open (O) or closed (C) channel state. (A and C) In the subactivating and inhibitory regimes, bursts of opening and closing events from fast conformational changes are interspersed with gaps from slower transitions. (B) In the optimal regime, the presence of modal gating means there is a capacity for channel closings of several seconds, even though the total P_O is high. Parameters are as in Table S2.

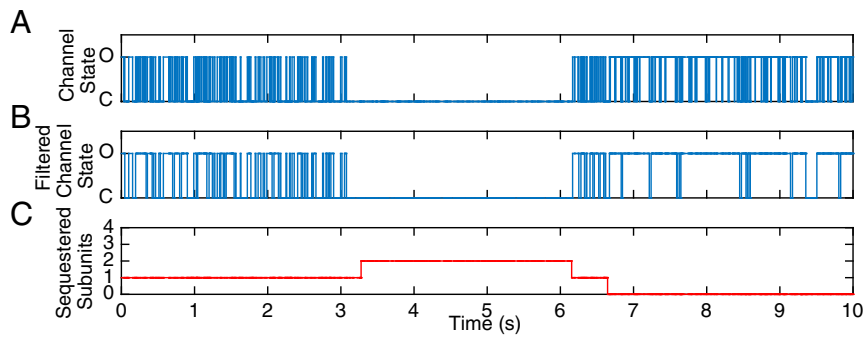


Fig. 5. Regulation of modal gating by slow sequestration of subunits. (A) An example of simulated gating at $1 \mu\text{M Ca}^{2+}$ concentration. (B) The trace is burst filtered to remove short closed events of duration less than $T_{\text{gmin}} = 15$ ms, revealing distinct modes of activity. (C) The number of sequestered subunits (those in states X_5, X_6 , or X_7) that underlie channel activity for this example simulation. Mode changes are a consequence of sequestering transitions regulating the availability of subunits for bursting. Parameters are as in Table S2.

bursts and gaps are produced by ligand-binding events at the activating and inhibitory sites. Slow suppression of a ligand-independent activation step means that at any point the channel may transition into an intermediate mode or longer-lived periods of quiescence. We now extend this to a full model of the IP₃R channel, including IP₃ binding and fitting parameters to stationary and transient kinetic data.

Full Model. Similar to the objectives of ref. 47, we aim to construct a gating model of type 1 IP₃R, regulated by both Ca^{2+} and IP₃, that can account for the following: equilibrium open probability (P_O), mean open time (τ_O) and closed time (τ_C), latency distributions for response to ligand concentration changes, and modal gating statistics (P_O^M, π^M, τ^M). We use the modal gating motif above as a basis, retaining the important timescale separation, and introduce IP₃ binding (with concentration denoted I) in a similar way to that of previous DYK schemes, renumbering rate constants accordingly (Fig. 6). We limit IP₃ binding to the non-sequestered, ligand-dependent component of the modal gating motif. The corresponding biophysical assumption is that the protein conformation that suppresses activation becomes available only after the change in structure resulting from IP₃ binding. We continue to assume sequential binding of activating and inhibitory Ca^{2+} , as has been suggested previously as a simplification of the DYK scheme (40). With these simplifying assumptions, we require only three additional states to be added to the modal gating motif and can account for almost all of the experimental data.

The normalization factor for this model is given by

$$Z = 1 + \frac{c}{K_6} \left(1 + \frac{c}{K_4} \right) + \frac{I}{K_7} \left(1 + \frac{1}{K_9} \right) + \frac{cI}{K_6 K_1} \left(1 + \frac{c}{K_2} + \frac{1}{K_9} + \frac{c}{K_2 K_{10}} + \frac{1}{K_{11}} \right), \quad [13]$$

and the open probability determined from Eq. 2 with $w_A = cI/K_6 K_1 K_{11} Z$ and $1 - w_A - w_C = (cI/K_6 K_1 Z)(1 + 1/K_9)$. Accounting for the two distinct open configurations with three active subunits, the equilibrium flux out of open states is given by $J = 4w_A^3 (1 - w_A - w_C) [3b_3 + (b_5 + ca_2 + b_1)/(1 + 1/K_9) + (b_5 + ca_8)/(1 + K_9)]$, which determines the mean open and closed times (Eq. 4).

Model Fitting. We perform a heuristic fit of the model to data taken from refs. 28 and 29, which was recorded from single type 1 IP₃Rs in native nuclear membrane of Sf9 insect cells. We use the equilibrium open probability to determine the dissociation constants for the model (Fig. 7A) and the mean open and closed

times to choose the rates a_{11} and b_{11} of fast conformational change to the active state (Fig. 7B and C). We use the remaining parameters to shape the transient dynamics of the system. To keep the number of parameters small we began by assuming the same symmetries in binding rates as in the modal gating motif and as in previous DYK schemes for the additional component. However, consideration of activation latencies led us to increase the rates between X_6 and X_9 compared with the other sequestering transitions and to introduce positive cooperativity in the rates of IP₃ and Ca^{2+} activation. Thus, in contrast to previous schemes, binding of IP₃ results in an increase in the activating Ca^{2+} binding and dissociation rates (and vice versa).

Ref. 29 characterized the transient behavior of the channel by recording the response of the IP₃R to rapid step changes in Ca^{2+} and IP₃ concentration. We fitted the model by comparing the experimental activation and recovery latency distributions to first passage times of the model. We calculate the cumulative distribution function (cdf) for the time to reach the set of open states from the initial condition given by the equilibrium distribution at the initial concentrations used in the experiments (*Materials and Methods*). We make an exception for the condition with initial concentrations $\text{Ca}^{2+} = 0 \mu\text{M}$ and $\text{IP}_3 = 10 \mu\text{M}$, in which all subunits are initialized in state X_4 . As discussed in ref. 47, because experimental ligand switches were performed 2 s after channel closing, there would have been insufficient time for the subunits to relax to state X_7 . We map the cdf to a logarithmically binned

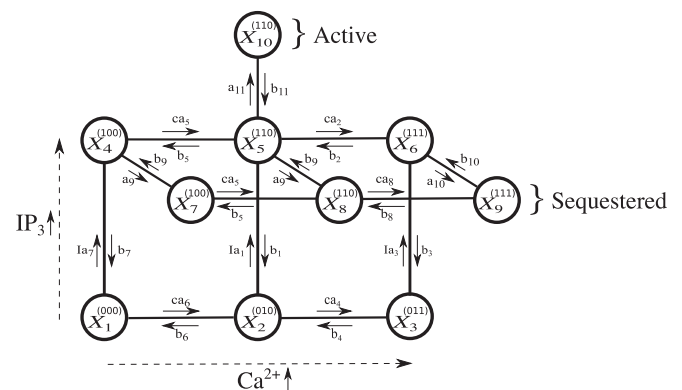


Fig. 6. Markov chain diagram of the full subunit model. Binding of IP₃, with concentration denoted I , has been introduced to the modal gating motif. The three digits in the superscripts correspond to the occupancy of the IP₃, activating Ca^{2+} , and inhibitory Ca^{2+} binding sites (consistent with the notation of the original DYK model). Parameter values are given in Table S3.

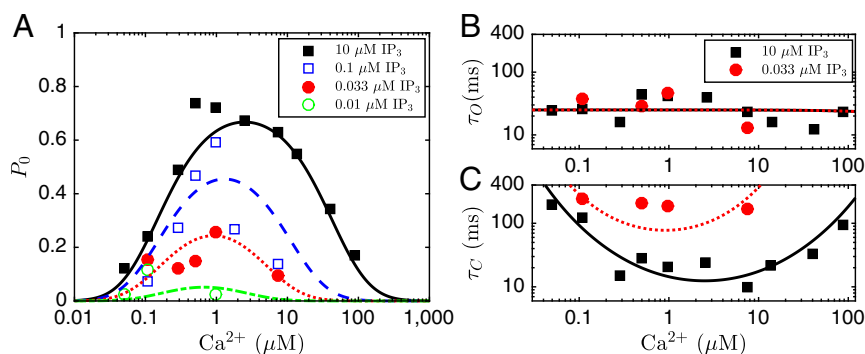


Fig. 7. Equilibrium properties of the full model as a function of Ca^{2+} and IP_3 concentration. (A) Open probability, (B) mean open time, and (C) mean closed time constrain the choices of dissociation constants and rates of conformational change to the active state. Curves are the theoretical fit to data taken from ref. 28 (symbols) at IP_3 concentrations of 10 μM (black), 0.1 μM (blue), 0.033 μM (red), and 0.01 μM (green).

histogram equivalent to those in refs. 29 and 47 to allow for direct comparison.

Even with a simple, heuristic fit, the model structure permits good agreement with the data. The model accounts for the three peaks in the latency histogram when activated from a condition of optimal $\text{Ca}^{2+} = 2 \mu\text{M}$ and $\text{IP}_3 = 0$ (Fig. 8A). This is a very interesting feature of the experimental data as it demonstrates that there are channel activation pathways on timescales spanning three orders of magnitude. In the context of the model, it is this timescale separation that leads to modal gating. The model Ca^{2+} activation latencies in saturating IP_3 (Fig. 8B) exhibit the same peak probability as the experimental data at ~ 10 – 30 ms, although with less variance. Simultaneous activation of the model with IP_3 and Ca^{2+} (Fig. 8C) also captures very well the primary component of the experimental latencies. The smaller component may be recovered by adding additional states to the model (e.g., more components of the original DYK scheme); however, as this has minimal influence on overall channel dynamics, we choose to keep the simpler model structure. Finally, the model captures the very long recovery latencies (mean ~ 2 s) after exposure to an inhibitory 300- μM Ca^{2+} concentration (Fig. 8D). The slow recovery was posited by ref. 29 to account for the similar refractory period observed between Ca^{2+} puffs *in vivo*.

Ref. 29 also reported deactivation and inhibition latencies, defined as the time taken for the channel to enter a closed state for a duration greater than 2 s, after a step change from optimal ligand concentrations (the reverse of conditions in Fig. 8). We cannot directly relate these distributions to first passage times of the model, so we generate the model distributions from simulations (Fig. S3). The fit to the data of IP_3 deactivation is very good, and although there is a discrepancy in the overall shape of the Ca^{2+} deactivation histograms, the model mean latency of 142 ms (in saturating IP_3) replicates the value of 160 ± 20 ms reported in ref. 29. Simultaneous removal of both Ca^{2+} and IP_3 yielded a longer mean deactivation latency for the model of 117 ms (experimental value 69 ± 5 ms), due to a smaller number of very short (1–10 ms) deactivations. When Ca^{2+} concentration is increased to 300 μM , the model channel inhibits more slowly (mean 527 ms) than in the experimental data (290 ± 40 ms) due to a higher proportion of long latencies, although it accounts for the primary component of the distribution to a good approximation.

Modal Gating Analysis. We consider the modal gating properties of the model at saturating and subactivating IP_3 concentrations of 10 μM and 0.033 μM , as examined experimentally by ref. 7. In the first case we define $\mathcal{B} = \{X_2, X_5, X_{10}\}$ and extend to $\mathcal{B} = \{X_2, X_4, X_5, X_{10}\}$ when $c > 5 \mu\text{M}$. Analogous to the above, we define $\mathcal{S} = \{X_8\}$, which extends to $\mathcal{S} = \{X_7, X_8\}$. The lower c threshold for inclusion of additional states in \mathcal{B} and \mathcal{S} in this

model is a consequence of the higher activation rate that came from model fitting. The sharp threshold naturally introduces a discontinuity, but the precise value does not affect the results. This gives

$$w_B = \frac{c}{K_6 Z} \left(1 + \frac{I}{K_1} + \frac{I}{K_1 K_{11}} \right) + \chi_{c>5} \frac{I}{K_7 Z} \quad [14]$$

$$w_S = \frac{cI}{K_6 K_1 K_9 Z} + \chi_{c>5} \frac{I}{K_7 K_9 Z} \quad [15]$$

$$w_{A|B} = \frac{1}{1 + K_{11} + \frac{K_1 K_{11}}{I} + \chi_{c>5} \frac{K_1 K_6 K_{11}}{c K_7}} \quad [16]$$

where $\chi_{c>5} = 1$ for $c > 5$ and zero otherwise. The partition of channel state space is defined as above for the modal gating motif. The case of subactivating IP_3 is similar, although we omit X_2 from \mathcal{B} because the time to reach the active state from X_2 becomes limited by slow IP_3 binding.

The decomposition of channel open probability (Fig. 9A) demonstrates the regulation of the channel by both of its ligands.

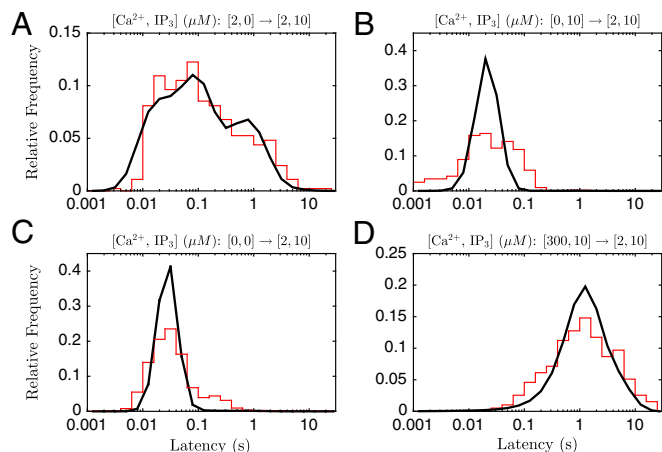


Fig. 8. Channel activation and recovery latencies. Shown is the distribution of time taken for channel opening after step changes from specified initial conditions (IC) to concentrations $[\text{Ca}^{2+}, \text{IP}_3] = [2 \mu\text{M}, 10 \mu\text{M}]$. (A) IC = $[2 \mu\text{M}, 0 \mu\text{M}]$, (B) IC = $[0 \mu\text{M}, 10 \mu\text{M}]$, (C) IC = $[0 \mu\text{M}, 0 \mu\text{M}]$, and (D) IC = $[300 \mu\text{M}, 10 \mu\text{M}]$. Distributions of the model (black) have been mapped to histograms with the same number of bins as the experimental data taken from ref. 29 (red).

Overall, the results suggest that the modal gating properties observable in traces of the binary channel state can indeed be ascribed to the underlying partitioning of the state space we have described. The Ca^{2+} dependence of modal gating revealed by segmentation at subactivating IP_3 (Fig. S6) also agrees with our theoretical results and predicts that within-mode open probabilities remain largely independent of both Ca^{2+} and IP_3 concentration.

Discussion

We have shown how ion channel modal gating can be understood at the level of subunit kinetics. We first considered two simple motifs for stochastic kinetics, showing how three distinct modes of channel activity can be understood in terms of a natural partition of the channel state space. From this we constructed a detailed model of the type 1 IP_3R that accounts for equilibrium channel properties, transient response kinetics, and modal gating. The model demonstrates that coupling of ligand binding and conformational change between subunits is not necessary for persistent time correlations in channel activity. Instead, modal gating is an emergent property that arises from a timescale separation in subunit kinetics.

Model Assumptions. As in previous subunit-based IP_3R models, we have assumed that at least three of four subunits must enter an active state for channel opening. However, we differ by considering separately the role of binding occupancy as a permissive factor. Whereas the necessity of full occupancy by IP_3 that we have included in the model has been established experimentally (48), the location of Ca^{2+} binding sites and stoichiometry of regulation are not yet known. In our model, each subunit must have an occupied activating Ca^{2+} site and an unoccupied inhibitory site for the channel to open. Although the steady-state channel properties can be suitably captured by the model if this assumption is relaxed, its enforcement accounts for several additional features of dynamic behavior.

Single-channel recordings at low Ca^{2+} and saturating IP_3 show abrupt and frequent switching between long channel closures and high activity bursts (7) (as in Fig. 4A). If opening were permissible in the model with only three occupied activating sites, then transitions in and out of bursts at low Ca^{2+} would instead exhibit short segments with I-mode kinetics. In the same way, channel closure from a single inhibited subunit in our model yields the isolated, high-activity bursts observable at high Ca^{2+} concentrations. As direct transitions between H and L are possible in the model from a single binding event, all three modes are completely interconnected, as described by ref. 7.

The updated rule for inhibition also addresses an issue that would otherwise likely arise from the fast conformational change our model shares with ref. 37. Although this component permitted ref. 37 an impressive fit to single-channel data, detailed simulations with dynamic Ca^{2+} feedback showed the time to termination of calcium puffs to be unreasonably long (42, 43). This is because the model requires the high Ca^{2+} concentration associated with an open channel pore to become inhibited, but can do so only from a closed state where the concentration quickly collapses to resting levels (34). Our model, however, which accounts accurately for both steady-state and transient data, inhibits directly from an open state. This should allow for appropriate puff termination by self-inhibition, as in the computational studies of refs. 41 and 50. Therefore, we argue that within this general framework the conditions we impose on Ca^{2+} regulation are the most consistent with IP_3R behavior and stand as a testable prediction of the model.

We interpret the separation of ligand-dependent and ligand-independent requirements for channel opening by analogy with the proposed gating mechanism for the ATP-sensitive K^+ channel (K_{ATP}). Conduction by the K_{ATP} is considered to be controlled by two gates: a slow, ligand-dependent gate formed by

constriction of the pore and a fast, ligand-independent gate associated with the selectivity filter (51). Ligand regulation determines the duration of bursts and gaps, with minimal effect on intraburst kinetics. Conversely, point mutations near the K_{ATP} selectivity filter alter the kinetics within bursts, but not the burst or gap durations (52). A similar mechanism has been suggested previously for the IP_3R to explain the upper bound on P_{O} in optimal ligand conditions (53) and appears consistent with the channel architecture. In a closed state each subunit contributes a transmembrane domain to constrict the channel pore, with each one linked to possible regulatory sites on the cytosolic side of the membrane (54). Ref. 54 also predicts a rearrangement of domains adjacent to the selectivity filter to allow the passage of Ca^{2+} . Thus, in our model, all subunits can be understood as necessary for opening a ligand-dependent gate, whereas three are sufficient to allow passage through a fast gate that controls the kinetics within bursts.

Modal gating emerges in the model from the interplay of the “3 out of 4” rule with a slow transition that leads to a set of sequestered states. Several consistent possibilities have been suggested to explain modal gating in other channels, such as phosphorylation (16, 17), binding of accessory proteins (13–15, 17, 20, 22, 24), ligand-independent conformational changes (13, 19), or alterations at the channel pore (18). Our model demonstrates that, in general, these mechanisms can act locally, by influencing even a single subunit, and that this is sufficient to generate the many distinct channel states assumed in whole-channel models.

Although the structure of the IP_3R is not known in sufficient detail to confirm or rule out such a mechanism, with the interpretation above, the model is testable at a more macroscopic level. Several mutations near the selectivity filter have been shown to inactivate the type 1 IP_3R (55). If the methods of ref. 48, which constructed channels with mutations in the IP_3 binding domain of a known number of subunits, can be extended to the mutations identified by ref. 55, then the model makes strong, parameter-free predictions of channel behavior. With one defective subunit, the model predicts a channel that gates only in I and L modes, given that the H mode requires four subunits. Similarly, with two defective subunits the model predicts that the channel gates only in L mode. More generally, a role for the selectivity filter suggests that IP_3R modal gating is subject to regulation from the luminal side of the ER membrane.

Role of IP_3R Modal Gating in Alzheimer’s Disease. The enhancement of IP_3R activity by mutant presenilins is a key contributor to the pathogenesis of familial Alzheimer’s disease. This is attributed to an increase in the prevalence of H mode, at the expense of L mode (12), leading to a disruption of Ca^{2+} homeostasis. This was recently examined using the whole-channel model of ref. 47. It was concluded that the mutation confers increased sensitivity of the channel to IP_3 , reflected in a change in occupancy of two particular aggregated states of the model (56). We cannot relate this result directly to our model, as although the model of ref. 47 incorporates putative ligand binding, it allows for a maximum of only three bound Ca^{2+} ions over the whole tetrameric channel. It is therefore unclear how the various aggregated states can be understood in terms of the underlying subunits of our model. Instead, we argue more directly from our model that interaction with mutant presenilins facilitates the IP_3 binding reaction.

The key evidence for this result is that the increase in channel P_{O} due to mutant presenilins was shown to be greater at subsaturating IP_3 concentration (11). Furthermore, experimental traces in ref. 12 show that channels exhibiting high P_{O} still exhibit long channel closures of several seconds. In the context of the model, this means that the slow sequestering transition must still be intact. Enhancement by facilitation of Ca^{2+} activation or relief of inhibition when IP_3 is bound is also unlikely. At the Ca^{2+}

concentration of 1 μM used in the experiments, activation is already close to saturation and inhibition is of little influence.

This leaves the possibility of either facilitation of IP_3 binding or relief of Ca^{2+} inhibition when IP_3 is unbound. We favor the former as a more direct mechanism and because it gives the more pronounced increase in π^{H} . In this regard, increasing the rate of IP_3 binding serves a dual purpose as it biases subunits more strongly toward the active state and allows more subunits to participate in bursts (i.e., $X_2 \in \mathcal{B}$ even at low IP_3 concentration). In terms of the equilibrium modal gating properties (Fig. 9), increasing the rate of IP_3 binding is equivalent to increasing the IP_3 concentration. Thus, the curves for the two IP_3 concentrations plotted in Fig. 9 demonstrate the effect of such a perturbation at subsaturating IP_3 : a large increase in P_{O} , greater prevalence of H mode, and decreased prevalence of L mode. This result is associated with a shorter mean closed time and an equivalent mean open time (Fig. 7), as seen experimentally (12).

Therefore, disruption of modal gating implicated in familial Alzheimer's disease does not require alteration of channel dynamics at the quaternary level, but rather just the kinetics of an elementary binding event. The model supports a hypothesis of an allosteric interaction between presenilins and IP_3R subunits in the membrane of the ER and suggests a search for sites of interaction near the IP_3 binding domain. The reasoning here depends only weakly on the parameters of the model and therefore encompasses the wide variety of cell types studied by ref. 12, regardless of differences in finer kinetic detail. Our model provides a useful tool to pursue this issue in concert with molecular studies and to explore further questions such as the potential connection to IP_3 sensitization by PKA (53) and cAMP (57).

Application to Other Ion Channels. Although modal gating is a ubiquitous feature of ion channel dynamics, it is unlikely that it has a universal origin (21). However, where there is strong evidence of a subunit-based mechanism, a compatible modeling approach will allow greater synergy between theory and experiment and serve to highlight commonalities. We discuss two such examples: G-protein-coupled inwardly rectifying potassium (GIRK) channels and large conductance calcium-activated potassium (BK) channels.

A subunit model can unify the mode switching behavior in GIRK1/4 channels that has been characterized at two different timescales. Four gating modes of GIRK1/4 channels in atrial myocytes were posited to arise directly from the independent binding of up to four G-protein $G_{\beta\gamma}$ subunits to the tetrameric channel (14, 15). At much longer timescales of tens of seconds, GIRK1/4 channels expressed in *Xenopus* oocytes switch between periods of high and low activity even at saturating $G_{\beta\gamma}$ (17). A recent whole-channel model was developed to account for the $G_{\beta\gamma}$ -dependent switching, although it did not account for the slow regulation (58). However, these are precisely the channel behaviors predicted by the modal gating motif, implemented without the constraint on ligand occupancy we assumed for the IP_3R . The ligand-dependent activation step in the motif accounts for the faster $G_{\beta\gamma}$ -dependent switching observed by refs. 14 and 15, whereas the slow sequestration incorporates the $G_{\beta\gamma}$ -independent regulation observed by ref. 17. An interesting point

of difference is that although the GIRK1/4 channel requires three functional subunits for opening (59), a greater number of modes were identified than for the IP_3R . This result raises the intriguing possibility that an additional mode is due to the heterotetrameric nature of the channel. If the two subunit types exhibit different kinetics, then two intermediate open probabilities would be expected, each relating to a particular composition of three contributing subunits. As our approach is easily generalized to heteromeric channels, the role of kinetic differences between subunit types can be explored directly in this and other channels.

BK channels in rat skeletal muscle have been found to exhibit four modes when held at constant voltage and Ca^{2+} concentration (13). Moving from the higher to lower open probability modes is associated with a restriction of a common state space and, in particular, a sequential removal of the longest-lived open states. As our decomposition of the IP_3R mean open time demonstrated, this is consistent with a model where the gating mode is determined by the number of contributing subunits. This hypothesis for BK channels can be tested with the detailed 50-state model of ref. 60, which characterizes gating in the highest (and most common) activity mode and explicitly represents the kinetics of four identical channel subunits. The hypothesis predicts that sequential removal of the subsets of the model corresponding to the highest number of contributing subunits will yield the gating activity observed in lower modes. A related question is whether the model structure of ref. 60 can be expressed more compactly in a form similar to our full IP_3R model (with voltage playing the role of IP_3 binding). Such a reduction would drastically reduce the number of free parameters (from 210 to ~ 20) and allow a systematic analysis of which features of channel behavior, if any, may require subunit cooperativity.

Materials and Methods

We investigate channel dynamics and perform simulations using the equivalent aggregated model that arises from the independent subunits and channel opening rule. Aggregated model states S_α are described by a multiindex $\alpha = (\alpha_1, \alpha_2, \dots, \alpha_n)$, with each α_i denoting the number of subunits in state X_i . An aggregated model derived in this way from k subunits with n subunit states will have a total of $\binom{n+k-1}{k}$ aggregated states. Two aggregated states S_α and S_β are connected if for some $i \neq j$, $\alpha_i - \beta_i = 1$ and $\alpha_j - \beta_j = -1$ and $\alpha_k - \beta_k = 0$ for all other components (i.e., one subunit has changed state). The flux from S_α to S_β is then given by $J_{\alpha\beta} = \alpha_i Q_{ij}$. The open states of the channel are those that satisfy the conditions described above.

We compute first passage time distributions used for model fitting, using the absorption method. We consider an initial distribution of aggregated states W_0 and the set of open states O . We denote by E_0 the vector whose components corresponding to open states are 1, and zero otherwise, and $\text{diag}(E_0)$ as the diagonal matrix with main diagonal E_0 . We denote the generator matrix for the aggregated model by A . We form the matrix $\tilde{A} = (\mathbb{I} - \text{diag}(E_0))A$, in which all of the elements of rows of A corresponding to O have been set to zero. The cdf of first passage times from W_0 to O is then given by the sum over open states of the solution to the Kolmogorov forward equation, $F_0(t) = W_0 e^{At} E_0^T$, which we evaluate numerically. Numerical work was performed using MATLAB (Mathworks).

ACKNOWLEDGMENTS. We thank Peter Dayan for valuable discussions. This work was supported by an Australian Postgraduate Award (to B.A.B.).

- Feske S (2007) Calcium signalling in lymphocyte activation and disease. *Nat Rev Immunol* 7(9):690–702.
- Rose CR, Konnerth A (2001) Stores not just for storage. Intracellular calcium release and synaptic plasticity. *Neuron* 31(4):519–522.
- Sutherland DJ, Pujic Z, Goodhill GJ (2014) Calcium signaling in axon guidance. *Trends Neurosci* 37(8):424–432.
- Orrenius S, Zhivotovskiy B, Nicotera P (2003) Regulation of cell death: The calcium-apoptosis link. *Nat Rev Mol Cell Biol* 4(7):552–565.
- Berridge MJ (1993) Inositol trisphosphate and calcium signalling. *Nature* 361(6410):315–325.
- Patterson RL, Boehning D, Snyder SH (2004) Inositol 1,4,5-trisphosphate receptors as signal integrators. *Annu Rev Biochem* 73(1):437–465.
- Ionescu L, et al. (2007) Mode switching is the major mechanism of ligand regulation of InsP_3 receptor calcium release channels. *J Gen Physiol* 130(6):631–645.
- Wagner LE, 2nd, Yule DI (2012) Differential regulation of the InsP_3 receptor type-1 and -2 single channel properties by InsP_3 , Ca^{2+} and ATP. *J Physiol* 590(14):3245–3259.
- Siekman I, Sneyd J, Crampin EJ (2014) Statistical analysis of modal gating in ion channels. *Proc R Soc A* 470:20140030.
- Siekman I, Cao P, Sneyd J, Crampin EJ (2015) Data-driven modeling of the inositol triphosphate receptor (IPR) and its role in calcium induced calcium release (CICR). arXiv:1507.06064.
- Cheung KH, et al. (2008) Mechanism of Ca^{2+} disruption in Alzheimer's disease by presenilin regulation of InsP_3 receptor channel gating. *Neuron* 58(6):871–883.
- Cheung KH, et al. (2010) Gain-of-function enhancement of IP_3 receptor modal gating by familial Alzheimer's disease-linked presenilin mutants in human cells and mouse neurons. *Sci Signal* 3(114):ra22.

13. McManus OB, Magleby KL (1988) Kinetic states and modes of single large-conductance calcium-activated potassium channels in cultured rat skeletal muscle. *J Physiol* 402(1):79–120.
14. Ivanova-Nikolova TT, Breitwieser GE (1997) Effector contributions to G $\beta\gamma$ -mediated signaling as revealed by muscarinic potassium channel gating. *J Gen Physiol* 109(2):245–253.
15. Ivanova-Nikolova TT, Nikolov EN, Hansen C, Robishaw JD (1998) Muscarinic K⁺ channels in the heart. Modal regulation by G protein $\beta\gamma$ subunits. *J Gen Physiol* 112(2):199–210.
16. Singer-Lahat D, Dascal N, Lotan I (1999) Modal behavior of the Kv1.1 channel conferred by the Kv β 1.1 subunit and its regulation by dephosphorylation of Kv1.1. *Pflügers Arch* 439(1–2):18–26.
17. Yakubovich D, Pastushenko V, Bitler A, Dessauer CW, Dascal N (2000) Slow modal gating of single G protein-activated K⁺ channels expressed in *Xenopus* oocytes. *J Physiol* 524(Pt 3):737–755.
18. Chakrapani S, et al. (2011) On the structural basis of modal gating behavior in K⁺ channels. *Nat Struct Mol Biol* 18(1):67–74.
19. Blatz AL, Magleby KL (1986) Quantitative description of three modes of activity of fast chloride channels from rat skeletal muscle. *J Physiol* 378:141–174.
20. Zhang W, Devi SPS, Tomita S, Howe JR (2014) Auxiliary proteins promote modal gating of AMPA- and kainate-type glutamate receptors. *Eur J Neurosci* 39(7):1138–1147.
21. Popescu GK (2012) Modes of glutamate receptor gating. *J Physiol* 590(1):73–91.
22. Delcour AH, Lipscombe D, Tsien RW (1993) Multiple modes of N-type calcium channel activity distinguished by differences in gating kinetics. *J Neurosci* 13(1):181–194.
23. Imredy JP, Yue DT (1994) Mechanism of Ca²⁺-sensitive inactivation of L-type Ca²⁺ channels. *Neuron* 12(6):1301–1318.
24. Luvisetto S, et al. (2004) Modal gating of human Ca_v2.1 (P/Q-type) calcium channels: I. The slow and the fast gating modes and their modulation by β subunits. *J Gen Physiol* 124(5):445–461.
25. Zahradníková A, Dura M, Györke S (1999) Modal gating transitions in cardiac ryanodine receptors during increases of Ca²⁺ concentration produced by photolysis of caged Ca²⁺. *Pflügers Arch Eur J Physiol* 438(3):283–288.
26. Rosales RA, Fill M, Escobar AL (2004) Calcium regulation of single ryanodine receptor channel gating analyzed using HMM/MCMC statistical methods. *J Gen Physiol* 123(5):533–553.
27. Taylor CW, et al. (2014) Structural organization of signalling to and from IP₃ receptors. *Biochem Soc Trans* 42(1):63–70.
28. Ionescu L, et al. (2006) Graded recruitment and inactivation of single InsP₃ receptor Ca²⁺-release channels: Implications for quantal [corrected] Ca²⁺ release. *J Physiol* 573(Pt 3):645–662.
29. Mak DOD, et al. (2007) Rapid ligand-regulated gating kinetics of single inositol 1,4,5-trisphosphate receptor Ca²⁺ release channels. *EMBO Rep* 8(11):1044–1051.
30. Mak DOD, Foscett JK (2015) Inositol 1,4,5-trisphosphate receptors in the endoplasmic reticulum: A single-channel point of view. *Cell Calcium* 58(1):67–78.
31. Bezprozvanny I, Watras J, Ehrlich BE (1991) Bell-shaped calcium-response curves of Ins(1,4,5)P₃- and calcium-gated channels from endoplasmic reticulum of cerebellum. *Nature* 351(6329):751–754.
32. Mak DO, McBride S, Foscett JK (1998) Inositol 1,4,5-trisphosphate [correction of trisphosphate] activation of inositol trisphosphate [correction of tris-phosphate] receptor Ca²⁺ channel by ligand tuning of Ca²⁺ inhibition. *Proc Natl Acad Sci USA* 95(26):15821–15825.
33. De Young GW, Keizer J (1992) A single-pool inositol 1,4,5-trisphosphate-receptor-based model for agonist-stimulated oscillations in Ca²⁺ concentration. *Proc Natl Acad Sci USA* 89(20):9895–9899.
34. Rüdiger S (2014) Stochastic models of intracellular calcium signals. *Phys Rep* 534(2):39–87.
35. Falcke M, Tsimring L, Levine H (2000) Stochastic spreading of intracellular Ca²⁺ release. *Phys Rev E Stat Phys Plasmas Fluids Relat Interdiscip Topics* 62(2 Pt B):2636–2643.
36. Yang J, Bruno WJ, Hlavacek WS, Pearson JE (2006) On imposing detailed balance in complex reaction mechanisms. *Biophys J* 91(3):1136–1141.
37. Shuai J, Pearson JE, Foscett JK, Mak DOD, Parker I (2007) A kinetic model of single and clustered IP₃ receptors in the absence of Ca²⁺ feedback. *Biophys J* 93(4):1151–1162.
38. Rüdiger S, et al. (2007) Hybrid stochastic and deterministic simulations of calcium blips. *Biophys J* 93(6):1847–1857.
39. Shuai J, Pearson JE, Parker I (2008) Modeling Ca²⁺ feedback on a single inositol 1,4,5-trisphosphate receptor and its modulation by Ca²⁺ buffers. *Biophys J* 95(8):3738–3752.
40. Shuai JW, Yang DP, Pearson JE, Rüdiger S (2009) An investigation of models of the IP₃R channel in *Xenopus* oocyte. *Chaos* 19(3):037105.
41. Rüdiger S, Shuai JW, Sokolov IM (2010) Law of mass action, detailed balance, and the modeling of calcium puffs. *Phys Rev Lett* 105(4):048103.
42. Rüdiger S, Nagaiah Ch, Warnecke G, Shuai JW (2010) Calcium domains around single and clustered IP₃ receptors and their modulation by buffers. *Biophys J* 99(1):3–12.
43. Swaminathan D, Jung P (2011) The role of agonist-independent conformational transformation (AICT) in IP₃ cluster behavior. *Cell Calcium* 49(3):145–152.
44. Rüdiger S, Jung P, Shuai JW (2012) Termination of Ca²⁺ release for clustered IP₃R channels. *PLoS Comput Biol* 8(5):e1002485.
45. Rückl M, et al. (2015) Modulation of elementary calcium release mediates a transition from puffs to waves in an IP₃R cluster model. *PLoS Comput Biol* 11(1):e1003965.
46. Cao P, Donovan G, Falcke M, Sneyd J (2013) A stochastic model of calcium puffs based on single-channel data. *Biophys J* 105(5):1133–1142.
47. Ullah G, Mak DOD, Pearson JE (2012) A data-driven model of a modal gated ion channel: The inositol 1,4,5-trisphosphate receptor in insect Sf9 cells. *J Gen Physiol* 140(2):159–173.
48. Alzayady KJ, et al. (2016) Defining the stoichiometry of inositol 1,4,5-trisphosphate binding required to initiate Ca²⁺ release. *Sci Signal* 9(422):ra35.
49. Colquhoun D, Hawkes AG (1982) On the stochastic properties of bursts of single ion channel openings and of clusters of bursts. *Philos Trans R Soc Lond B Biol Sci* 300(1098):1–59.
50. Ullah G, Parker I, Mak DOD, Pearson JE (2012) Multi-scale data-driven modeling and observation of calcium puffs. *Cell Calcium* 52(2):152–160.
51. Nichols CG (2006) KATP channels as molecular sensors of cellular metabolism. *Nature* 440(7083):470–476.
52. Proks P, Capener CE, Jones P, Ashcroft FM (2001) Mutations within the P-loop of Kir6.2 modulate the intraburst kinetics of the ATP-sensitive potassium channel. *J Gen Physiol* 118(4):341–353.
53. Foscett JK, White C, Cheung KH, Mak DOD (2007) Inositol trisphosphate receptor Ca²⁺ release channels. *Physiol Rev* 87(2):593–658.
54. Fan G, et al. (2015) Gating machinery of InsP₃R channels revealed by electron cryo-microscopy. *Nature* 527(7578):336–341.
55. Schug ZT, et al. (2008) Molecular characterization of the inositol 1,4,5-trisphosphate receptor pore-forming segment. *J Biol Chem* 283(5):2939–2948.
56. Mak DOD, Cheung KH, Toglia P, Foscett JK, Ullah G (2015) Analyzing and quantifying the gain-of-function enhancement of IP₃ receptor gating by familial Alzheimer's disease-causing mutants in Presenilins. *PLoS Comput Biol* 11(10):e1004529.
57. Tovey SC, et al. (2010) Regulation of inositol 1,4,5-trisphosphate receptors by cAMP independent of cAMP-dependent protein kinase. *J Biol Chem* 285(17):12979–12989.
58. Yakubovich D, et al. (2015) A quantitative model of the GIRK1/2 channel reveals that its basal and evoked activities are controlled by unequal stoichiometry of G_α and G $\beta\gamma$. *PLoS Comput Biol* 11(11):e1004598.
59. Sadja R, Alagem N, Reuveny E (2002) Graded contribution of the G $\beta\gamma$ binding domains to GIRK channel activation. *Proc Natl Acad Sci USA* 99(16):10783–10788.
60. Rothberg BS, Magleby KL (2000) Voltage and Ca²⁺ activation of single large-conductance Ca²⁺-activated K⁺ channels described by a two-tiered allosteric gating mechanism. *J Gen Physiol* 116(1):75–99.
61. Norris JR (1998) *Markov Chains* (Cambridge Univ Press, Cambridge, UK).

Supporting Information

Bicknell and Goodhill 10.1073/pnas.1604090113

SI Materials and Methods

Conditional Mean Open Time. In the main text we noted for the modal gating motif that the mean open time in H mode is longer than that of I mode by a factor of 2. Here we provide details of the calculation and the expressions plotted in Fig. 3D of the main text.

We calculate mean open times by using an equivalent aggregated representation of the model. Because the subunits are assumed to be independent, the channel states can be grouped into complexes based on the total number of subunits populating each subunit state (*Materials and Methods*). The aggregated representation of the modal gating motif has 210 channel states, of which 3 are open. All open states have three active subunits, but are distinguished by the state of the fourth. We use the shorthand O_k to denote an open state with the distinguishing subunit in X_k , so for example O_6 corresponds to the single I-mode open state. Channel openings begin as the channel enters either O_2 or O_6 from a closed state and may then involve a transition to O_4 , which has all subunits active. Conditional on beginning in each O_k , the mean channel open times $\langle\tau_{O_k}\rangle$ can be calculated as mean first passage times to the set of closed states that communicate directly with the open states.

Using standard methods (ref. 61, section 3.3), we find

$$\langle\tau_{O_4}\rangle = \frac{1}{4b_3} + \langle\tau_{O_2}\rangle \quad [\text{S1}]$$

$$\langle\tau_{O_2}\rangle = \frac{1}{3b_3 + a_3 + b_1 + ca_2 + a_4} + \frac{a_3}{3b_3 + a_3 + b_1 + ca_2 + a_4} \langle\tau_{O_4}\rangle + \frac{a_4}{3b_3 + a_3 + b_1 + ca_2 + a_4} \langle\tau_{O_6}\rangle \quad [\text{S2}]$$

$$\langle\tau_{O_6}\rangle = \frac{1}{3b_3 + b_1 + ca_2 + b_4} + \frac{b_4}{3b_3 + b_1 + ca_2 + b_4} \langle\tau_{O_2}\rangle. \quad [\text{S3}]$$

Because the rates a_4, b_4 are assumed slow, the first term dominates in Eq. S3. This gives $\langle\tau_{O_6}\rangle \sim 1/3b_3$ for I-mode openings, because the rate b_3 is assumed faster than ligand binding or dissociation. The first two terms dominate in Eq. S2, accounting for the fact that sojourn to O_4 is likely before closing. Solving the equations gives $\langle\tau_{O_2}\rangle$ explicitly as

$$\langle\tau_{O_2}\rangle = \frac{1 + a_3/4b_3 + a_4/(3b_3 + b_1 + ca_2 + b_4)}{3b_3 + b_1 + ca_2 + a_4 - a_4b_4/(3b_3 + b_1 + ca_2 + b_4)}. \quad [\text{S4}]$$

Thus, we have $\langle\tau_{O_2}\rangle \sim 2/3b_3$, giving a factor of 2 increase in mean open time for H mode compared with I mode.

The two quantities given by Eqs. S3 and S4 are plotted in Fig. 3D of the main text. Weighting these by the conditional probability of being in O_6 or O_2 , given the channel has just opened, gives a decomposition of mean open time

$$\langle\tau_O\rangle = \frac{w_6}{1 - w_A - w_C} \langle\tau_O^I\rangle + \frac{w_2}{1 - w_A - w_C} \langle\tau_O^H\rangle. \quad [\text{S5}]$$

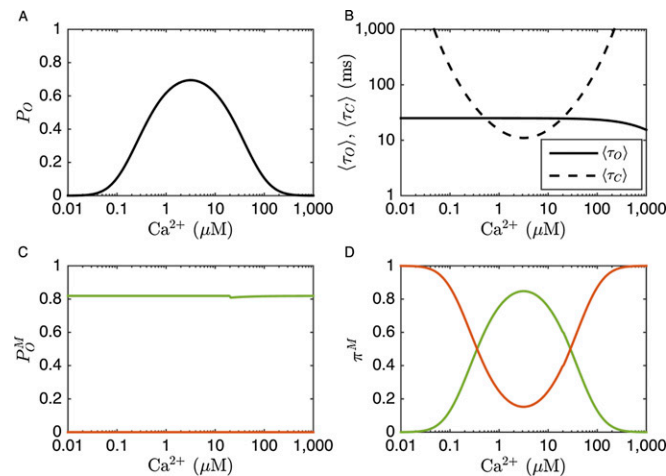


Fig. S1. Equilibrium properties of the bursting motif. The average behavior of the channel can be understood in terms of the time spent in a bursting (H, green) or quiescent (L, red) state. (A) The total channel open probability P_O (black line) exhibits the characteristic bell-shaped Ca^{2+} dependence. (B) The short mean open time $\langle\tau_O\rangle$ reflects the fast kinetics within bursts. The mean closed time $\langle\tau_C\rangle$ is much larger at subactivating and inhibitory concentrations, which exhibit longer gap durations. (C) Within-mode open probabilities P_O^M are ligand independent. (D) The proportion of time spent in each mode π^M is strongly ligand dependent. The total open probability can be expressed in terms of the time spent in H as $P_O = \pi^H P_O^H$.

Table S3. Full model parameters

| Parameter | Value | Parameter | Value, s ⁻¹ |
|-----------|--|-----------|------------------------------|
| a_1 | $50 \mu\text{M}^{-1} \cdot \text{s}^{-1}$ | b_1 | 2.5 |
| a_2 | $0.035 \mu\text{M}^{-1} \cdot \text{s}^{-1}$ | b_2 | 1.25 |
| a_3 | $\frac{b_3 K_4}{K_1 K_2} \mu\text{M}^{-1} \cdot \text{s}^{-1}$ | b_3 | 0.25 |
| a_4 | $3.5 \mu\text{M}^{-1} \cdot \text{s}^{-1}$ | b_4 | 12.5 |
| a_5 | $65 \mu\text{M}^{-1} \cdot \text{s}^{-1}$ | b_5 | 10 |
| a_6 | $25 \mu\text{M}^{-1} \cdot \text{s}^{-1}$ | b_6 | $\frac{a_6 K_5 K_7}{K_1}$ |
| a_7 | $10 \mu\text{M}^{-1} \cdot \text{s}^{-1}$ | b_7 | 0.25 |
| a_8 | $0.035 \mu\text{M}^{-1} \cdot \text{s}^{-1}$ | b_8 | $\frac{a_8 K_2 K_{10}}{K_9}$ |
| a_9 | 0.15 s^{-1} | b_9 | 0.2 |
| a_{10} | 1.25 s^{-1} | b_{10} | 2.5 |
| a_{11} | 110 s^{-1} | b_{11} | 20 |

$K_i = b_i/a_i$ are the dissociation constants, used here to enforce detailed balance.